Chapter 7
Structure and Interactions of Polymer Thin Films from Infrared Ellipsometry

Andreas Furchner

Abstract Polymer films play a vital role in technological, industrial, and biomedical applications. Prominent examples are protective anti-fouling coatings, bio/chemical sensors and devices, organic electronics, as well as functional films with tunable surface characteristics. The films' physical and chemical properties strongly correlate with structure and interactions, which also drive function and functionality. Infrared-spectroscopic ellipsometry (IR-SE) enables comprehensive investigations of those properties, as the IR spectral range contains structure-sensitive baselines and material-specific vibrational bands. In situ IR-SE is a powerful monitoring tool for film chemistry in dependence of stimuli like temperature, humidity, solvent type, pH, and solute concentration. Combined with optical modeling, IR-SE can quantitatively probe numerous film properties, such as chemical composition, anisotropy, molecular orientation, thickness, hydration, and molecular interactions. Recent advances of polymer-film characterization are presented in this chapter, showing, among others, various examples from our group *In Situ Spectroscopy* at ISAS Berlin in collaboration with IPF Dresden, including investigations of polymer film composition and orientation, protein adsorption on functional surfaces, swelling behavior of polymer brushes, and molecular interactions in hydrated polymer films.

7.1 Introduction

A variety of spectroscopic methods exists for probing the properties of polymers[1–4]. Visible (VIS) ellipsometry, for example, is widely and successfully used to characterize thin polymer films in dry and swollen states (see Chaps. 5, 6, 8, 9, 12, 15, and 16). This chapter deals with infrared ellipsometry, a complementary but powerful polarization-dependent spectroscopic technique for ex situ and in situ investigations of complex polymer thin films. Determining spectroscopically the structural

A. Furchner (✉)
Leibniz-Institut für Analytische Wissenschaften – ISAS – e.V.,
Schwarzschildstraße 8, 12489 Berlin, Germany
e-mail: andreas.furchner@isas.de

K. Hinrichs and K.-J. Eichhorn (eds.), *Ellipsometry of Functional Organic Surfaces and Films*, Springer Series in Surface Sciences 52,
https://doi.org/10.1007/978-3-319-75895-4_7

properties of such films—like blends, multilayers, and mixed brushes—relies on having a significant spectral contrast, that is, a sufficiently large enough difference in the optical constants n (and k) of the individual film constituents. Many transparent polymers with Cauchy-like dispersions in the visible spectral range have rather similar refractive indices. The presence of vibrational bands in the infrared often provides substantially higher contrasts, rendering the IR an important region to probe. Moreover, band positions, amplitudes, and shapes are closely linked to numerous physical and chemical film properties. Besides its obvious application to determine a film's optical constants [5–16] (see Chaps. 23 and 24), IR-SE can therefore be employed to access, and consequently better unterstand, such properties including specific chemical bonds, tacticity, molecular orientation, conformation, local chemical environments, and molecular interactions.

Measured IR-SE spectra are quantitatively interpreted via optical multilayer models based on thicknesses and dielectric functions of the individual layers. For many polymer films their IR dielectric function can be described by a sum of vibrational oscillators,

$$\varepsilon(\tilde{\nu}) = \varepsilon_\infty + \sum_i \varepsilon_i^{\mathrm{vib}}(\tilde{\nu}), \tag{7.1}$$

each of which is characterized by position, amplitude, and shape parameters. Here, $n_\infty = \sqrt{\varepsilon_\infty}$ is the high-frequency refractive index. While typical IR bands are of Lorentzian shape, molecular groups involved in interactions like hydrogen bonding tend to be associated with Gaussian-shaped oscillators because of line broadening due to the increased number of local chemical environments. Voigt oscillators [17, 18], with their two line-shape parameters to quantify shapes between the Lorentzian and Gaussian extremes, are suitable for modeling complex band compositions in interacting polymer systems.

Composite and/or hydrated polymer layers can be modeled based on effective-medium theories (see Chap. 1). The effective dielectric function of a hydrated film, for instance, may be calculated according to Bruggeman [19, 20] from the dielectric properties of water and dry polymer,

$$0 = f_{\mathrm{H_2O}} \frac{\varepsilon_{\mathrm{H_2O}} - \varepsilon_{\mathrm{eff}}}{\varepsilon_{\mathrm{H_2O}} + 2\varepsilon_{\mathrm{eff}}} + (1 - f_{\mathrm{H_2O}}) \frac{\varepsilon_{\mathrm{Polymer}} - \varepsilon_{\mathrm{eff}}}{\varepsilon_{\mathrm{Polymer}} + 2\varepsilon_{\mathrm{eff}}}. \tag{7.2}$$

If the polymer interacts with water, the polymer dielectric function needs to be modified by introducing corresponding additional oscillators, which then allow a simultaneous fit on film thickness, hydration ($f_{\mathrm{H_2O}}$), and molecular interactions [21]. Film anisotropy, accounted for by replacing the scalar dielectric functions by tensors, can be handled using generalized matrix algorithms (Chap. 1).

To illustrate how IR-SE can probe specific properties of polymer films, this chapter will first give several brief examples concerning composition and molecular orientation of dry films. Afterwards, in situ examples of hydrated polymer films and brushes in aqueous environments will be discussed, focusing on identification, monitoring, and quantification of changes in film structure and molecular interactions.

7.2 Composition

Morphology, composition, miscibility, interdiffusion, and interactions at interfaces are important quantities of polymer surfaces, blends, and complex polymer composite films. Because of the high material-specific spectral contrast in the infrared, IR-SE is highly advantageous for the determination of said properties.

Interdiffusion [22] and cross-linking [23], which often occur during aging or thermal annealing of polymers, are particularly important processes to understand. They depend, among others, on structure and interactions of the individual polymers, and are therefore readily detectable via the vibrational fingerprint. Typical infrared marker bands for this purpose are associated with carbonyl, nitrile, amine, ether, ester, or hydroxyl vibrations, but also with ring and backbone vibrations. Monitoring position, amplitude, and shape of these bands provides plenty of qualitative and semiquantitative insights into the properties of the polymer–polymer interface, such as chemical changes during cross-linking. For a detailed and quantitative characterization, optical modeling can be utilized, yielding properties like the interfacial width in miscible and partially miscible polymer systems.

IR-SE was used, for instance, to quantify the annealing-induced mixing in a polymeric layered system of PnBMA [poly(*n*-butyl methacrylate)] and PVC [poly(vinyl chloride)] [24]. The authors measured the CO and CC stretching vibrational bands of PnBMA between 1100–1300 cm^{-1}, which are sensitive toward molecular interactions of the polymer's ester groups and therefore toward conformational changes upon annealing [25]. Based on optical modeling of individual PnBMA and PVC layers, as well as annealed, completely mixed films, it was possible to distinguish, for partially annealed PnBMA/PVC films, between a bilayer of the two polymers and a three-layer system with an interdiffusion middle layer (see Fig. 7.1).

A similar approach was used by Duckworth et al. [26] to detect whether interdiffusion or complete mixing occured between thin films of PMMA [poly(methyl methacrylate)] and PVDF [poly(vinylidene fluoride)]. Their analysis exploited the dependency of PMMA-specific carbonyl and PVDF-specific CF_2 bands on annealing and molecular interactions between the two polymers.

Besides determining the depth composition of a layered system, IR-SE can also be employed for investigating the lateral makeup of complex polymer films. Ionov et al. [27] quantified the chemical composition of an 8 nm thin 1D gradient mixed polymer brush prepared from PS [polystyrene] and PBA [poly(*tert*-butyl acrylate)]. The two polymers were grafted onto a polymer anchoring monolayer by utilizing a heating stage for annealing that produces a temperature gradient across the substrate's surface, thereby gradually varying the grafting properties. The resulting gradient brush was then chemically mapped for PS- and PBA-specific vibrational bands (see Fig. 7.2). PBA's carbonyl stretching band around 1730 cm^{-1} provided a high spectral contrast to the ring vibrations of PS at lower wavenumbers, allowing the determination of the brush composition. A line shape analysis of PBA's carbonyl band in principle also enables one to study how molecular interactions are related to local composition, that is, how PBA–PBA and PBA–PS interactions impact brush

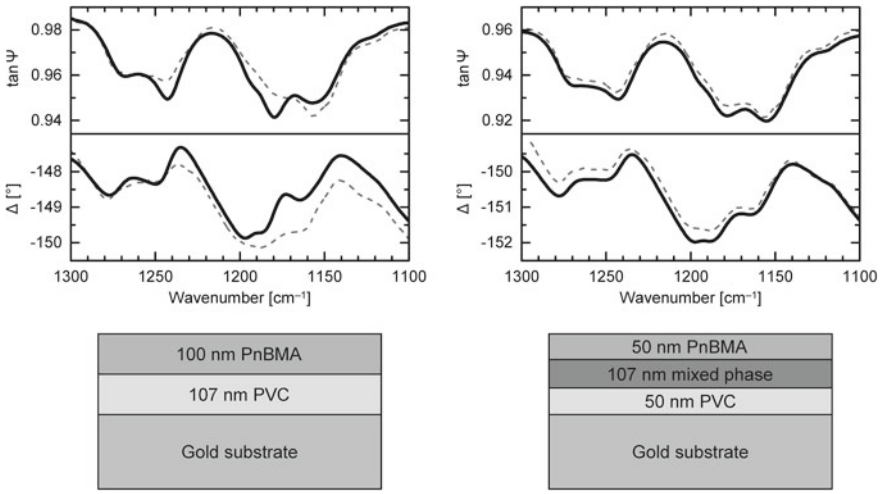

Fig. 7.1 Measured (dashed) and simulated (solid) IR-SE spectra of partially annealed PnBMA/PVC films (data from [24]). Left: Bilayer model for a 30 min annealed film. Right: Three-layer model accounting for interdiffusion in a 10 min annealed film

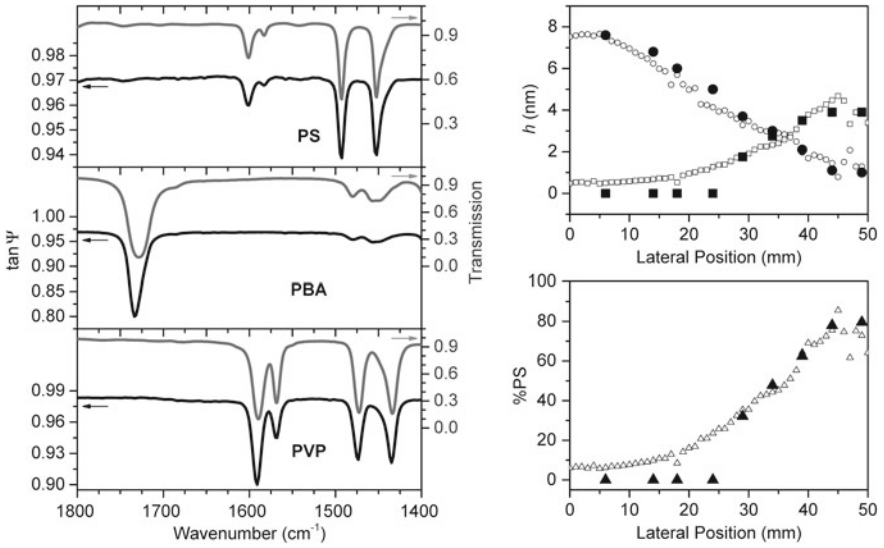

Fig. 7.2 Left: Reference IR-SE tanψ (and transmission) spectra of PS, PBA, and PVP [poly(2-vinylpyridine)] for the determination of local brush composition. Right: Laterally resolved relative thickness contributions *h* of PS (squares) and PBA (circles) in an 8 nm thin gradient PS-*mix*-PBA brush, as well as relative PS volume percentages %PS across the gradient. Closed and open symbols are data from IR-SE and single-wavelength VIS ellipsometry, respectively. Adapted with permission from [27]. Copyright (2005) American Chemical Society

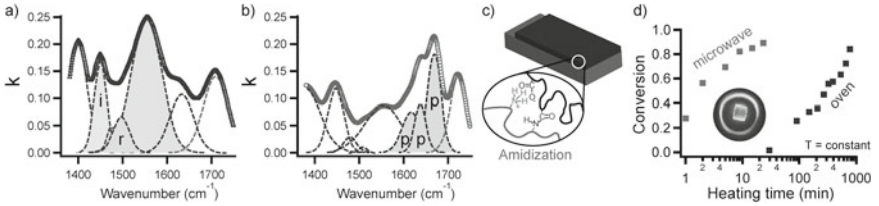

Fig. 7.3 Amidization reaction in BPEI/PAA multilayers monitored with IR-SE. Absorption coefficient before (**a**) and after (**b**) cross-linking, amidization scheme (**c**) and kinetics (**d**) upon microwave and conventional heating. Adapted from [28]. Copyright (2016), with permission from Elsevier

properties like thickness and grafting density. Such an analysis will be the topic of Sect. 7.4.4.

Concerning cross-linking reactions at polymer–polymer interfaces, IR-SE is a valuable composition monitoring and quantification tool. Lin et al. [28] investigated the cross-linking reaction of BPEI/PAA [branched polyethylenimine/poly(acrylic acid)] multilayer films. As shown in Fig. 7.3, the authors extracted the absorption index k from IR-SE data between 1350–1750 cm^{-1} using nine vibrational oscillators in the optical model. Besides CH bending modes, which did not change during the reaction, these oscillators are associated with vibrations of antisymmetric (1399 cm^{-1}) and symmetric (1552 cm^{-1}) COO^- stretching, COOH stretching (1707 cm^{-1}), NH_3^+ deformation (1496 cm^{-1}), NH bending (1632 cm^{-1}), as well as amide I related modes around 1670 cm^{-1}. The latter become visible as NH_3^+ and COO^- groups react to form amide groups (HNCO). This amidization reaction could be induced by conventional heating, or by microwave heating with accelerated reaction kinetics.

Similarly, Simpson et al. [29] followed the formation of covalent Si–O–C bonds upon the reaction between carboxylic acid groups of PAA and silyl (SiH) groups in a vinyl-terminated poly(dimethyl siloxane) cross-linker. They stress that incomplete cross-linking could lead to the continued presence of reactive SiH groups in silicone coatings, causing "lock-up" problems in silicone–acrylic adhesive laminates.

Being able to probe and quantify the individual film constituents is also very valuable for studying effects like film contamination. Bungay et al. [6] investigated silicone films for potential solvent residues. They spincoated 100 nm thick films onto optically thick gold films using CV-1144-O silicone thinned with VM&P Naphtha, a solvent containing different hydrocarbons. Using IR-SE combined with a Bruggeman effective-medium approximation (7.2) to model the film's dielectric function, the residual Naphtha concentration was found to be merely (0.5 ± 0.3) vol%. As shown in Fig. 7.4, this sensitivity was possible because of the characteristic CH_x bands of Naphtha between 2700 and 3200 cm^{-1}.

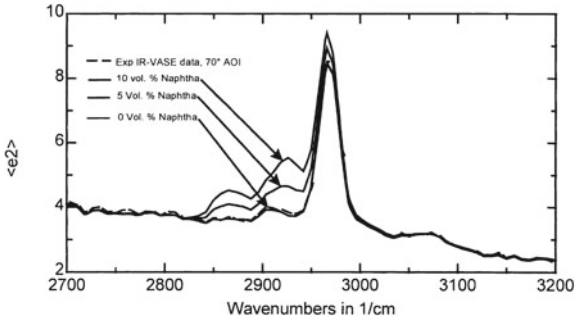

Fig. 7.4 Measured (dashed) imaginary pseudo-dielectric function of a 100 nm thick CV-1144-O silicone film compared to calculations (solid) based on different concentrations of residual Naphtha solvent within the film. Reprinted from [6]. Copyright (1998), with permission from Elsevier

7.3 Molecular Orientation

Direct access to the vibrational properties of thin films renders infrared ellipsometry particularly suitable for studying molecular orientation, conformation, packing density, and structure in general. These properties can manifest themselves as anisotropy in the sample's optical response and can therefore be probed with polarized light. While uniaxial film anisotropy can be addressed by ellipsometric measurements at various incidence angles, or by individual p- and s-polarized reflectance measurements, resolving biaxial anisotropy naturally requires additional data at different in-plane sample rotations. However, with regard to molecular orientation, knowledge about film chemistry and direction of transition dipole moments can significantly simplify the infrared analysis, as will be demonstrated later.

Molecular orientation plays an important role in a variety of (polymer) thin-film systems. An instructive example are self-assembled monolayers (SAMs) [30, 31] (see also Chaps. 4 and 9). These ultrathin films usually consist of a head group for anchoring to a substrate, a spacer or tail section, and—if desired for the specific application—a functional end group. It is often the orientation and density of those end groups that are crucial for a successful subsequent functionalization of the monolayer. Typical SAM structural models are depicted in Fig. 7.5. They account for properties like packing density, chain tilt, and chain order, all of which can be explored in the infrared.

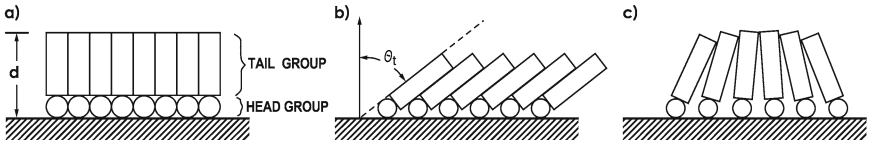

Fig. 7.5 Structural models of an organized monolayer assembly with closest packed arrangement of head groups and **a** tail groups oriented normal to the substrate surface, **b** tail groups uniformly oriented at an angle θ, and **c** a distribution of tilted tail groups. Adapted with permission from [32]. Copyright (1987) American Chemical Society

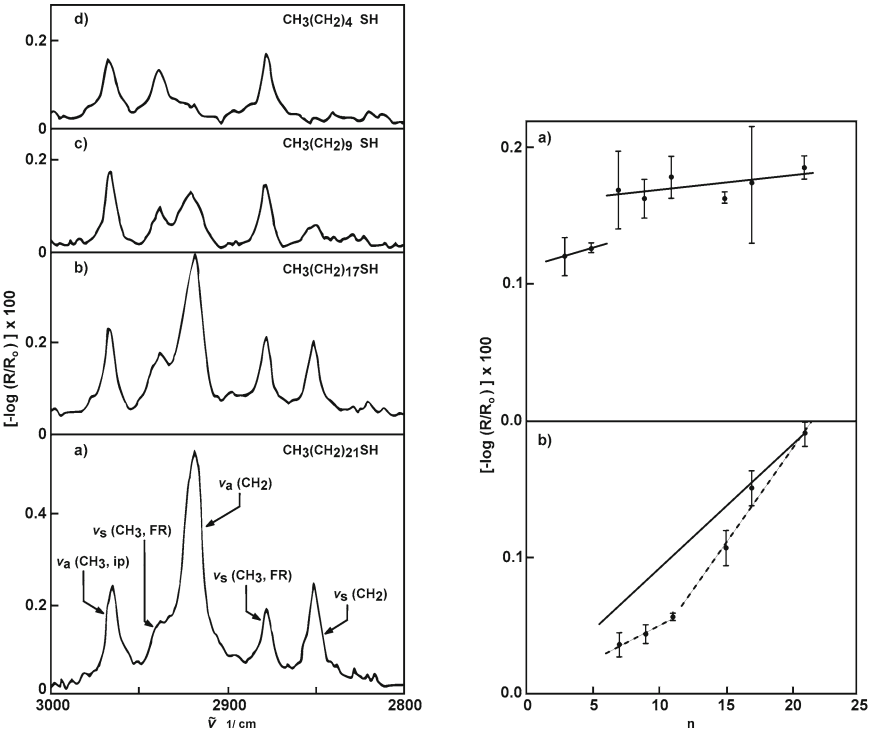

Fig. 7.6 Left: p-polarized reflection spectra in the methyl and methylene stretching region of self-assembled n-alkyl thiol monolayers on gold. Right: Peak heights of $\nu_a(CH_{3,ip})$ (**a**) and $\nu_s(CH_2)$ (**b**) bands versus number n of methylene groups. Solid lines in (**a**) are to guide the eye. Solid line in (**b**) is a linear interpolation from the origin. Adapted with permission from [32]. Copyright (1987) American Chemical Society

Infrared spectroscopy was extensively used for studying the structural properties of SAMs [32–35]. Porter et al. [32] used polarized IR spectroscopy to investigate—besides film uniformity, structural integrity, and packing density—the molecular orientation of SAMs, as well as the local chemical environment within the films. They probed the CH_x stretching region of self-assembled n-alkyl thiol monolayers $[CH_3(CH_2)_nSH]$ on gold, with a number of repeating methylene units between $n = 1$ and 21. Comparing the CH_x peak positions of the monolayers (Fig. 7.6, left) with those of crystalline polymethylene chains (with $n = 21$) and the liquid state (with $n = 7$) provided insights into the local chemical environment of a chain. In monolayers with methylene chain lengths $n > 11$, the peak positions correspond to those of the bulk crystalline phase, whereas for shorter chains with $n < 11$, they resemble those of the liquid phase. Moreover, for alkyl chains with consistent chain orientation, it is expected that the band intensities of the $\nu(CH_2)$ methylene stretching vibrations increase linearly with n, whereas those of the $\nu(CH_3)$ methyl end group's stretching vibrations remain constant. However, a different situation was found (Fig. 7.6, right),

again with a characteristic change in trends around $n = 11$ repeating units (dashed lines). The authors explained the deviations from the linear behavior with differences in average tilt angle and structure. For long-chain monolayers with $n = 15$–21, they found a tilt of about 20–30°, corresponding to a structure similar to that in Fig. 7.5b. Short-chain monolayers with $n < 11$, on the other hand, tend toward slightly higher tilt angles, which they explained by a more disordered chain distribution with decreased packing density and coverage.

A similar study [33] on self-assembled n-alkyl thiol monolayers on silver substrates revealed quite different structural properties. For chains longer than about $n = 10$, monolayers were predominantly densely packed and crystalline-like with all-trans conformational sequences that exhibited average tilt angles of about 13°. More tilted structures were hypothesized for shorter-chain monolayers. The smaller tilt angles on silver compared to gold hint at differences in the bonding of the sulfur head group, which was further substantiated by contact-angle measurements.

Deducing the molecular orientation from polarized IR spectra is based on simple trigonometric considerations of the involved transition dipole moments [36, 37]. In all-trans hydrocarbon chains, for instance, the chain axis and the transition dipole moments of the $\nu_{as}(CH_2)$ and $\nu_s(CH_2)$ stretching vibrations are mutually orthogonal. The chain's tilt angle θ from the surface normal is therefore given by [1]

$$\cos^2\theta + \cos^2\theta_{as} + \cos^2\theta_s = 1. \tag{7.3}$$

The angles θ_{as} and θ_s of the two methylene stretching vibrations can be measured via their transition dipole moments

$$\begin{aligned} M_{i,x}^2 &= M_{i,\max}^2 \cdot \sin^2\theta_i \cdot \cos^2\phi_i, \\ M_{i,y}^2 &= M_{i,\max}^2 \cdot \sin^2\theta_i \cdot \sin^2\phi_i, \\ M_{i,z}^2 &= M_{i,\max}^2 \cdot \cos^2\theta_i, \end{aligned} \tag{7.4}$$

which are proportional to the respective oscillator strengths computable in an optical model. Here, $M_{\max}$ is the principle transition dipole moment, and ϕ is the in-plane rotation of a chain. In a uniaxial film, for which $\overline{\cos^2\phi} = \overline{\sin^2\phi} = 1/2$, the average tilt angle of both symmetric and antisymmetric methylene stretching vibrations can then be calculated from

$$\frac{M_{i,x}^2}{M_{i,z}^2} = \frac{\sin^2\theta_i}{2\cos^2\theta_i}, \tag{7.5}$$

allowing one to deduce the chain's tilt angle θ via (7.3).

Using this approach, Rosu et al. [35] determined average chain tilts of 19 and 22° for hexadecanethiol on gallium arsenide and gold, respectively, suggesting a similar organizational structure on both substrates. Monolayers of octanedithiol on GaAs, by contrast, were found to be more disordered with average tilt angles of 30°.

Note that band interpretation is rather straightforward for thin films on metals like silver or gold. Owing to the metal surface selection rule [2], only transition dipole

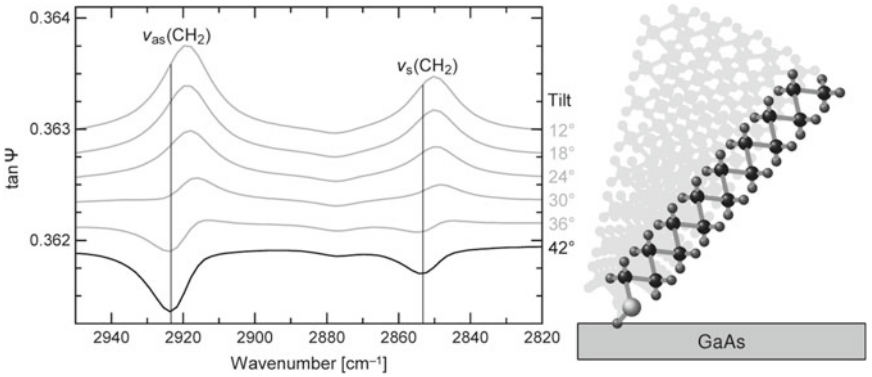

Fig. 7.7 Calculated tan Ψ spectra of hexadecanethiol self-assembled monolayers on GaAs in dependence of average tilt angle. Data from [35]

components perpendicular to the metal's surface can be observed in a spectrum. The measured band intensities can therefore be directly related with the chain's tilt angle. For arbitrary substrates, though, band positions and line shapes can vary quite dramatically. This is demonstrated in Fig. 7.7 illustrating the sensitivity of IR-SE toward tilt-angle variations. The graph shows calculated tan Ψ spectra of hexadecanethiol on GaAs with heavily tilt-dependent $\nu_{as}(CH_2)$ and $\nu_s(CH_2)$ band amplitudes, positions, and line shapes. The two vertical lines, which indicate the center frequencies of the corresponding oscillators in the optical model, highlight an important circumstance that any IR spectroscopist should internalize: The frequency of a measured peak does not necessarily coincide with the oscillator's resonance frequency!

Another interesting example concerning structure and molecular orientation is that of Langmuir–Blodgett (LB) films. Such films are composed of organic monolayers deposited from the surface of a liquid onto a substrate via immersion or emersion. Tsankov et al. [38] investigated the influence of thermal annealing on the structural properties of LB films consisting of multiple double layers of 2-[4-(*N*-dodecanoylamino)phenyl]-5-(4-nitrophenyl)-1,3,4-oxadiazole on gold. The molecule, depicted in Fig. 7.8, has a nonlinear shape with its diphenyl oxadiazole fragment being bent in the molecular plane and twisted with respect to the aliphatic tail. The tails themselves are connected to benzene rings via amide groups, which can facilitate hydrogen bonds between neighboring chains. Strong hydrogen bonds could be inferred from the well-pronounced stretching bands related to bonded NH (3325 cm^{-1}) and C=O groups (1680 cm^{-1}). Those bonds were only partly disrupted after film annealing at 130 °C. However, the $\nu(CH_2)$ bands diminished in amplitude upon annealing, suggesting molecular rearrangements of the chains. In particular, the observed frequency upshifts by 4 cm^{-1} could be attributed to an all-trans–gauche conformational transformation. Annealing also resulted in a thickness increase from 60 to 65 nm, hinting at a lowering of the overall molecular tilt angle. This was verified by a tilt-angle determination of the molecule's nitro

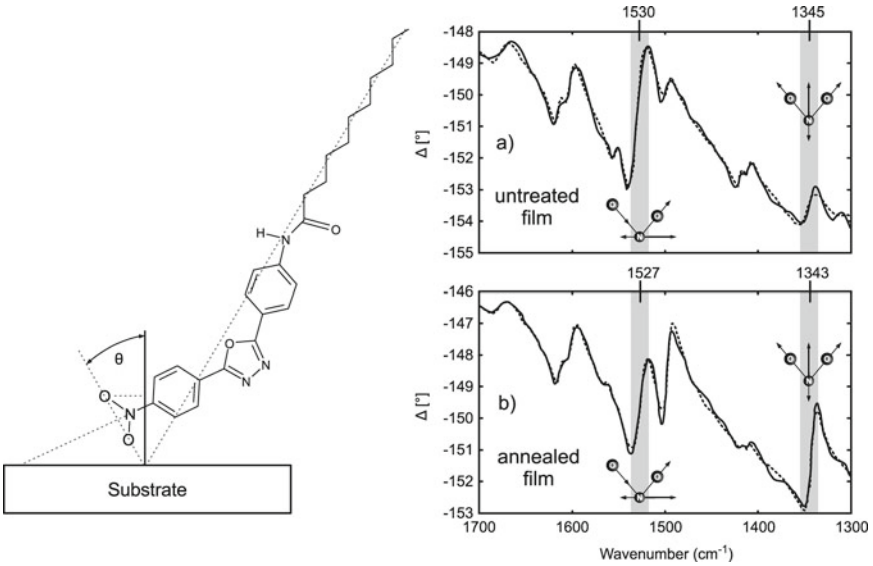

Fig. 7.8 Left: Molecular orientation of the studied Langmuir–Blodgett film (see text). Right: Measured (solid) and fitted (dashed) Δ spectra in the NO_2 stretching region before (**a**) and after (**b**) annealing at 130 °C. Adapted with permission from [38], copyright (2002) American Chemical Society; and from [39], copyright (1998), with permission from Elsevier

head group (angle θ in Fig. 7.8). Fitting the symmetric and antisymmetric stretching vibrations of NO_2 groups at 1345 and 1530 cm^{-1}, respectively, the authors found a marked change in tilt angle from 39° for the untreated film to 53° for the annealed film.

One last example of out-of-plane uniaxially anisotropic films are dicyanovinyl-sexithiophene films for photovoltaic applications. A comprehensive IR-SE study revealed that the molecular orientation undergoes changes with increasing film thickness [40]. An isotropic distribution of orientations with an average tilt of 55° (close to the so-called magic angle of 54.7°) was characteristic for 4 nm thin films consisting of about two or three monolayers. Thicker films of 20 nm showed preferential in-plane molecular orientation with average tilt angles of 67°. Such higher tilts are favorable when using sexithiophene as absorber material in organic solar cells, resulting in enhanced photon absorption and thus charge-carrier generation.

Seemingly biaxially anisotropic polymer films are depicted in Fig. 7.9, showing the in-plane anisotropy of stretched PET [poly(ethylene terephthalate)] and PEN [poly(ethylene naphthalate)] films [12]—two materials with relevance for flexible electronic devices. These polymers have several characteristic vibrational modes with transition dipole moments along or normal to the chain axis, hence the observed enhanced or diminished band amplitudes at corresponding sample rotations. While ethylene-glycol wagging (1340 cm^{-1}) and the complex ester modes (1260 cm^{-1}, 1080–1160 cm^{-1}) are parallel to the chain axis, the C=O stretching

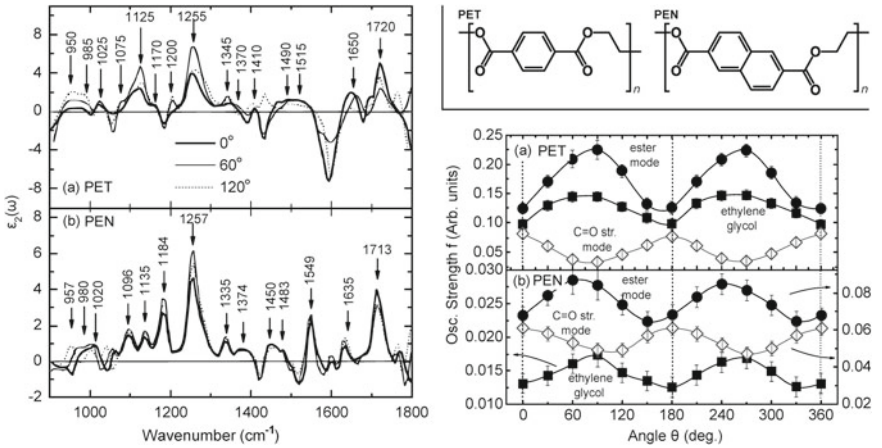

Fig. 7.9 Left: Imaginary part of the dielectric function of PET and PEN films at 0° (bold line), 60° (solid line), and 120° (dotted line) in-plane sample rotation. Bottom-right: Angular dependence of the oscillator strength of ethylene glycol (squares), ester (circles), and C=O (diamonds) stretching modes. Reprinted from [12], with the permission of AIP Publishing. Top-right: Chemical structures of PET and PEN

mode (1720 cm^{-1}) is perpendicular to it, as is evident from the projected oscillator strengths (Fig. 7.9, bottom-right). Perhaps unsurprisingly for stretch-oriented films, a refractive-index analysis revealed that both PET and PEN films can be treated as uniaxial materials with their optical axis parallel to their surface.

For further reading on molecular orientation in organic thin films, the reader is referred to Chaps. 3, 13, 20, and 21.

7.4 Hydrated Polymer Films

Examples of thin films shown so far dealt with non-hydrated layers under ambient conditions in air. In the following, hydrated films are addressed that are exposed either to air with significant humidity levels or to aqueous environments, including salt and protein solutions. In situ IR-SE on such solid–liquid interfaces is very useful for qualitative and semi-quantitative studies. It was, for instance, successfully applied for monitoring the adsorption of proteins on functional surfaces [41], the pH-responsive dissociation of polyelectrolyte films [42] and mixed brushes [44], the swelling behavior and interactions of end-grafted polyoxazoline brushes [43], the chemical and structural changes during the complex formation of mixed anionic/cationic polyelectrolyte brushes [45], the electrochemical growth of polypyrrole films [46], as well as the hydrophilicity of complex composite polymer surfaces to tune hydrophobic interactions [47]. First quantitative approaches proved promising for modeling the electrochemical grafting of nanometer-thin nitrobenzene [48] and maleimide multi-

layers [49], the growth process of PSS-doped polyaniline films [50], as well as the swelling–deswelling transition of polyacrylamide brushes [51].

The full potential of in situ IR-SE as an analytical technique became apparent with the use of optical models to gain quantitative information about film hydration, structure, and molecular interactions [21]. This combination of IR-SE and optical modeling enabled detailed quantitative investigations of hydrated polymer films at the solid–liquid interface, and was used, for example, for studying the role of molecular interactions in the stimuli-responsive phase transition of polymer brushes [21].

Before diving into the details of quantitative in situ IR-SE, a typical experimental set-up of ellipsometer plus flow cell will be introduced, followed by examples of polymer films in aqueous environments, with a particular focus on polymer brushes. Their densely grafted polymer chains give rise to fascinating surface properties susceptible to changes induced by external stimuli like temperature or pH changes (see Chap. 6).

7.4.1 In Situ Infrared Ellipsometry

In situ IR-SE measurements of solid–vapor or solid–liquid interfaces demand precise control of humidity, temperature, solvent, pH, and other possibly influential environmental parameters. Special in situ cells are thus required. Figure 7.10 shows an example of a temperature-controlled flow cell [41, 44] in an in situ infrared ellipsometer. The cell itself, including in- and outlet tubes, consists of organic polymers like PEEK (polyether ether ketone) or PTFE (polytetrafluorethylen) that exhibit excellent chemical resistance properties needed for measurements in low- or high-pH solutions. A quartz window at the back of the cell allows the possibility to implement additional simultaneous in situ optical techniques like VIS reflection anisotropy spectroscopy [46] (see Chap. 1). Temperature of the cell can be regulated between 15–50 °C with a stability of ±0.05 °C. This precision is imperative because the optical properties of solvents like water are strongly temperature dependent. The whole set-up is purged with dry air to guarantee constant atmospheric conditions and to reduce absorption of IR radiation by atmospheric water vapor.

The polymer film (or any other film for that matter) is prepared on the inner side of the actual window substrate. This might be done either *ex situ* or directly from solution within the cell. The substrate, made from an IR-transparent material like Si or CaF_2, has a wedge-shaped form that ensures well-separated inner and outer reflexes preventing interferences from multiple internal reflections. The flow cell can also be modified with electrodes in order to do electrochemistry experiments while performing in situ IR-SE [46].

Note that the configuration in Fig. 7.10 probes the solid–liquid interface under non-ATR conditions. Compared with ATR, the shorter pathlength through the substrate allows access to a wider spectral range (8000–700 cm^{-1} for Si) with retained phase coherence necessary for accurate phase measurements Δ. Depending on external incidence angle at, and refractive index of, the substrate, internal incidence angles

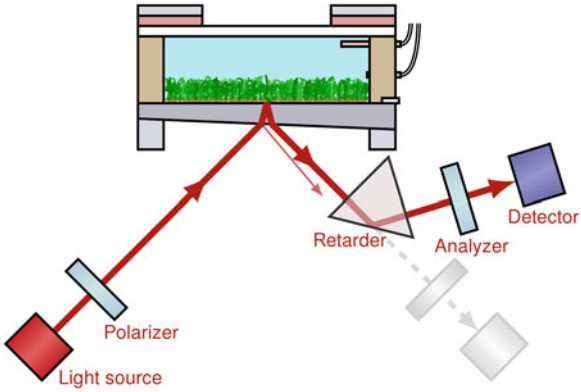

Fig. 7.10 Schematic of an in situ polarizer/sample/retarder/analyzer IR-SE set-up with temperature-controlled flow cell and infrared-transparent, wedge-shaped window substrate [44]. Depending on film and solvent properties, measurements with and/or without retarder can be performed for sensitive phase determination

between 5–16° at the substrate/film interface are feasible. This non-zero angle ensures sensitivity toward thin-film thickness and out-of-plane anisotropy [44].

7.4.2 Polymer Films and Brushes in Aqueous Environments

Ellipsometric spectra of isotropic polymer films in aqueous environments are dominated by the strong vibrational bands of water that often mask the film signature of interest. This is demonstrated in Fig. 7.11 (left) for thin PGMA [poly(glycidyl methacrylate)] films on Si. While the polymer bands of thicker films are clearly visible, the vibrational features of the 2 nm ultrathin film are buried beneath the water stretching and bending modes. Spectral referencing can circumvent this problem by significantly enhancing the optical contrast. One way of referencing is with respect to spectra of a clean substrate (without polymer film) obtained under similar, or same, well-defined experimental conditions as the film spectra. This approach is often necessary when the solvent's optical properties change during the experiment and again cause too drastic an overlap with the film signature, as is the case, for instance, in temperature-dependent studies. As shown in Fig. 7.11 (right) for the PGMA films, this approach makes visible even the bands of the 2 nm ultrathin film. Another way is self-referencing where ratios $\tan\Psi / \tan\Psi_0$ and differences $\Delta - \Delta_0$ are recorded with respect to the initial conditions of an in situ experiment, such as the film's state before a protein-deposition study or before exposure to pH variations. Any changes from, respectively, unity and zero are then associated with changes in the optical properties of the solid–liquid interface.

The first straightforward example of an in situ study is presented in Fig. 7.12. In this combined investigation using IR-SE and VIS ellipsometry (see also Chap. 6), the proteins fibrinogen (FIB) and human serum albumin (HSA) were tested for their adsorption behavior on various polymer surfaces, namely a $d_{\mathrm{dry}} = 2.5$ nm ultrathin hydrophobic PGMA film, a 14.5 nm thin hydrophilic PNIPAAm brush, a 25.1 nm

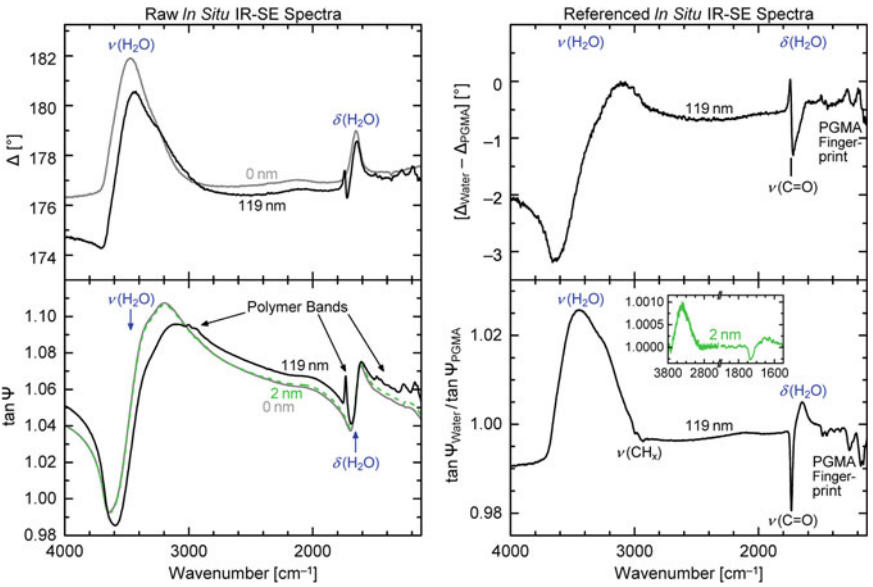

Fig. 7.11 Left: Raw IR-SE spectra of 0, 2, and 119 nm thick PGMA films in H_2O. Right: Same spectra referenced to a clean silicon wedge ("0 nm" on the left)

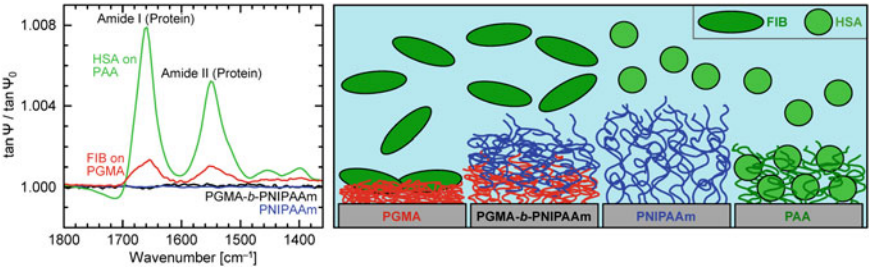

Fig. 7.12 Self-referenced IR-SE spectra showing protein adsorption and repellent behavior of different polymer (brush) surfaces with respect to fibrinogen (FIB) and human serum albumin (HSA). Initial conditions were protein-free aqueous solutions. The polymer films consist of PGMA [poly(glycidyl methacrylate)], PNIPAAm [poly(*N*-isopropylacrylamide)], PGMA-*b*-PNIPAAm, and PAA [poly(acrylic acid)]. Adapted with permission from [41]. Copyright (2015) American Chemical Society

thick PGMA-*b*-PNIPAAm block-copolymer brush, and a 6.9 nm thin PAA polyelectrolyte brush [41]. The self-referenced spectra exhibit upward-pointing protein-related amide I and amide II bands showing that FIB and HSA adsorbed on PGMA film and PAA brush, respectively. The measured amide band amplitudes correspond to monolayer FIB adsorption on top of PGMA, whereas for PAA they indicate that HSA penetrates into the brush and thereby adsorbs in more copious amounts, in accordance with VIS ellipsometry (26 mg/m^2 HSA at pH 5). The shapes of FIB's

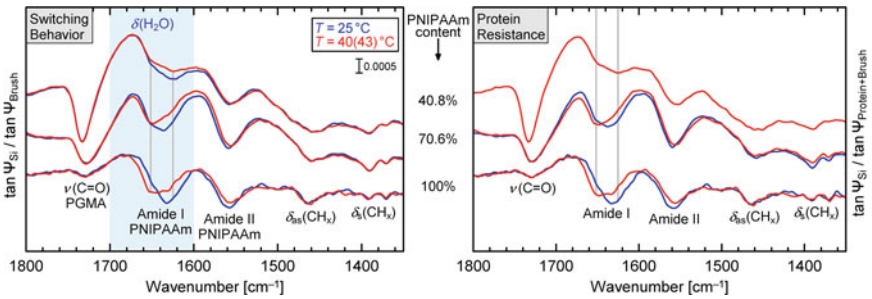

Fig. 7.13 Left: Cascaded temperature-dependent in situ spectra of a pure PNIPAAm brush (100%, $d = 14.5$ nm dry thickness) and PNIPAAm-*b*-PGMA brushes with 70.6% ($d = 26.8$ nm) and 40.8% ($d = 25.1$ nm) PNIPAAm content measured in protein-free solution. The upward-pointing $\delta(H_2O)$ band overlaps the amide I bands redshifting their indicated band components (vertical lines) in dependence of brush thickness and hydration. Right: Corresponding spectra of pure PNIPAAm brush in HSA solution and PNIPAAm-*b*-PGMA copolymer brushes in FIB solution. Adapted with permission from [41]. Copyright (2015) American Chemical Society

and HSA's amide bands are dictated by the proteins' secondary structures. Different hydrogen-bond patterns, such as alpha-helices or beta-sheets within the proteins, have characteristic impacts on line shape and band composition, often leading to complex amide bands with multiple subbands. A closer analysis of the measured amide bands in Fig. 7.12—in comparison to transmission measurements of protein solutions—revealed that the proteins did not change their structure during adsorption from the solution. This is crucial information for applications that rely on the integrity of the adsorbed molecules.

Being pH-responsive polyelectrolytes [42], PAA brushes can be triggered via changes in solvent pH to ad- and desorb proteins. Such processes were monitored time-dependently with in situ IR-SE, showing good agreement with brush thickness and amount of adsorbed protein determined by VIS ellipsometry [41].

Contrary to PGMA and PAA, both the pure PNIPAAm brush and the PGMA-*b*-PNIPAAm copolymer brush turned out to be resistant toward FIB and HSA adsorption (surface concentration $\ll 0.5$ mg/m^2). This repellent behavior was unexpected for the copolymer surface because the idea behind creating those mixed brushes was to obtain thermoresponsive films switchable between a protein repellent and a non-repellent state. The protein-repellent PNIPAAm toplayer was thought to be collapsable via temperature stimulus, thereby surface-exposing the PGMA sublayer that is able to bind proteins. To test whether this switching behavior does occur, several brushes with varying PGMA/PNIPAAm composition were measured below and above PNIPAAm's swelling–deswelling transition temperature [41]. Results are given in Fig. 7.13 (left). Because of referencing with respect to a clean wedge, the data show downward-pointing polymer bands—predominantly the amide I/II and CH_x-bending bands of PNIPAAm, and the carbonyl band of PGMA—overlapped by the upward-pointing water bending mode around 1650 cm^{-1}. PNIPAAm's amide I band, which is mainly associated with C=O stretching, contains at least two major

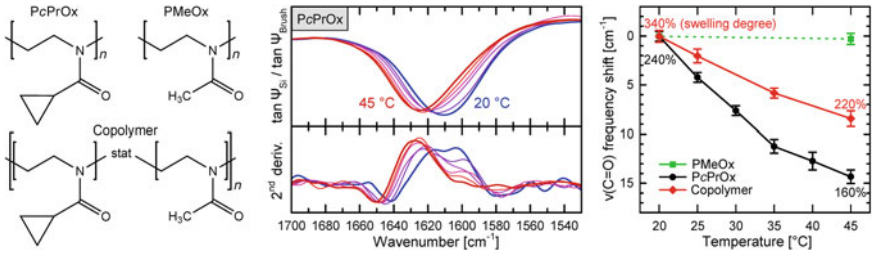

Fig. 7.14 Left: Chemical structures of PMeOx, P*c*PrOx, and their statistical copolymer. Middle: IR-SE spectra, and their 2nd derivative, of the ν(C=O) band of a P*c*PrOx brush in D_2O measured at 20, 25, . . ., 45 °C. Right: Relative ν(C=O) upshift (with respect to band maximum at 20 °C) in the three types of polymer brushes compared with swelling degree obtained from VIS ellipsometry. Adapted from [43] in accordance with the Creative Commons Attribution (CC BY) license

components. One, observed at about 1625 cm^{-1}, is related to carbonyl moieties fully hydrated by water molecules, whereas the other one at about 1652 cm^{-1} stems in part from C=O groups hydrogen-bonded to H–N moieties of neighboring amide groups. The pure PNIPAAm brush exhibits marked alterations between these two components with increasing temperature, indicating the brush's collapse. This switching behavior is seen to a lesser extent, or not at all, the lower the PNIPAAm content is in the copolymer brushes. These mixed brushes therefore do not collapse like a classical PNIPAAm brush, which can be explained by their structural properties. Cross-linking between different PGMA segments during brush preparation probably causes parts of the PNIPAAm blocks to emerge from within the PGMA sublayer rather than from its surface, resulting in molecular interactions and steric hindrance between PNIPAAm and PGMA in the PGMA/PNIPAAm interpenetration layer, and consequently in a less pronounced swelling–deswelling transition. No differences were observed when comparing the spectra with measurements of the same brushes exposed to protein solutions (Fig. 7.13, right). In other words, no protein adsorption took place on any of the PNIPAAm-containing polymer films because PNIPAAm always dominated their surface properties.

Kroning et al. also investigated molecular interactions in temperature-responsive oxazoline-based polymer brushes between 20–45 °C in H_2O and D_2O. Specifically, they studied carbonyl–water hydrogen bonding in P*c*PrOx [poly(2-cyclopropyl-2-oxazoline)] and PMeOx [poly(2-methyl-2-oxazoline)] brushes, as well as in copolymer brushes containing 75% *c*PrOx and 25% MeOx. Being ternary amides (see Fig. 7.14), these polymers do not contain N–H groups that could facilitate intra- or intermolecular hydrogen bonds with carbonyl groups. The measured amide I carbonyl bands are therefore comprised of comparitively few subbands related to the differently hydrogen-bonded C=O species. The first subband, associated with free C=O, is seen in the dry but not in the hydrated state in water. The other two subbands are connected with weakly and strongly hydrated C=O groups, implying that all of the brushes' carbonyl groups are at least partially hydrated when exposed to water. For the pure P*c*PrOx brush, the temperature-dependent second derivative of the tan Ψ

carbonyl band shows a transition between the two major band components, that is, between stronger hydration at lower temperatures and weaker hydration at higher temperatures. This transition is not as pronounced for the copolymer brush with its lower relative content of temperature-responsive P*c*PrOx.

As depicted in Fig. 7.14 (right), the measured C=O-stretching transitions compare well with changes in swelling degree determined from VIS ellipsometry. Contrary to the steplike transition of thermoresponsive polymers like PNIPAAm [52], the P*c*PrOx and copolymer brushes showed continuous ν(C=O) upshifts with increasing temperature, correlating with less polymer–water interactions within the collapsing brushes. Smaller band shifts, but higher swelling degrees, were observed for the copolymer brush, meaning that more water molecules are retained in the copolymer brush because of its higher hydrophilicity. Put another way, the more pronounced the measured C=O transition the stronger the thickness transition, highlighting the close correlation between molecular interactions and brush deswelling. In fact, the nonresponsive and more hydrophilic PMeOx can be used to tune the transition behavior of the copolymer system [53], rendering these types of poly(2-oxazoline) brushes highly interesting for potential applications.

7.4.3 Optical Effects and the Role of Water Bands

Nontrivial baselines and spectral overlaps between polymer and water vibrational bands can cause serious problems with regard to data interpretation of transmission and ATR infrared spectra. A common example is the amide I band of peptides and proteins, which is heavily masked by the water bending mode. One way to reveal the true amide band shapes is to use heavy water, the vibrational bands of which occur at much lower wavenumbers compared to normal water. Figure 7.15 illustrates this with IR-SE measurements of a PNIPAAm brush around its swelling–deswelling temperature in H_2O and D_2O. As discussed before, during the brush's collapse around 32 °C, the amide I band undergoes a transition between two major components associated with hydrated C=O groups at lower temperatures and amide-interacting C=O groups at higher temperatures. Not only are the corresponding vibrational oscillators redshifted in D_2O, but the actual transition is less sharp. It extends over a larger temperature range because D_2O forms stronger hydrogen bonds than H_2O. Also in more complex polymer systems like proteins, such stronger bonds can potentially influence the film's structural, and thereby functional, properties.

Other strategies to deal with band-overlap and baseline issues are solvent background subtraction and baseline correction methods [2, 54]. The aim is always to suppress, or get rid of, the solvent bands and other unwanted "artifacts" in order to obtain pure polymer spectra suitable for qualititave interpretation, or for quantitative evaluation via oscillator band fits. These strategies, however, can cause serious errors in band interpretations and should thus be avoided whenever possible.

A fundamentally different approach is to use optical models to compare measured with calculated spectra, as is routinely done with ellipsometry. As alluded to in the

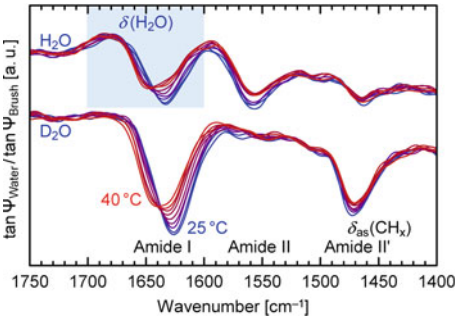

Fig. 7.15 Amide I/II/II' bands during the temperature-induced swelling–deswelling transition of a PNIPAAm brush in H_2O and D_2O. Note the absence of an amide II band for the deuterated brush. The amide I overlap with $\delta(H_2O)$ causes smaller apparent band amplitudes

beginning, these models for interpretation of infrared spectra are based on a chemical, physical, and optical description of the hydrated films, automatically accounting for optical effects like baseline drifts due to thin-film interference, band-shape distortions due to n/k mixing, and dielectric effective-medium effects from film hydration [2, 20, 55]. The models do not rely on manipulation procedures like certain ATR corrections or subtraction of solvent background, and therefore allow a more accurate quantitative interpretation of measured spectra.

To illustrate why optical modeling is a powerful tool, it is useful to recall that referenced in situ IR-SE spectra measure the optical contrast of the solid–liquid interface. As shown in Fig. 7.16, derivative-like bands appear in Δ upon referencing, whereas absorption-band-like downward-pointing film-related bands and upward-pointing solvent-related bands manifest in $\tan\Psi$. Again, it has to be stressed that the observed water bands and baseline drifts are simply a result of the optical contrast between film-on-substrate and no-film-on-substrate data. Any change in the optical properties of the solid–liquid interface will therefore immediately affect bands and baselines [44], rendering them important markers for detecting minute changes of the film's properties. Specifically, amplitude and line shape of both film and solvent bands strongly depend on incidence angle, film swelling, hydration, and complex refractive index. Particularly in the case of water, with its very strong and broad absorption bands, it therefore makes obvious sense not to ignore or remove those bands but to include them in a fit in order to gain a better quantitative understanding of said film properties.

Rappich and Hinrichs were the first to attempt to reproduce the water vibrational bands by optical modeling. They monitored the growth of ultrathin nitrobenzene films on H-passivated Si(111) wedges from a solution of 4-nitrobenzenediazonium-tetrafluoroborate during the electrochemical processing in diluted sulfuric acid (see Chap. 20 for details). As shown in Fig. 7.17, the presence of symmetric and antisymmetric NO_2 stretching bands is clear evidence for successful grafting. Using ellipsometrically determined optical constants of water, they compared the measured nitrobenzene film spectrum to calculated spectra based on a non-hydrated film with varying thickness d and high-frequency refractive index n_∞ (7.1). Although the agreement is not perfect—probably due to small but non-negligible film anisotropy

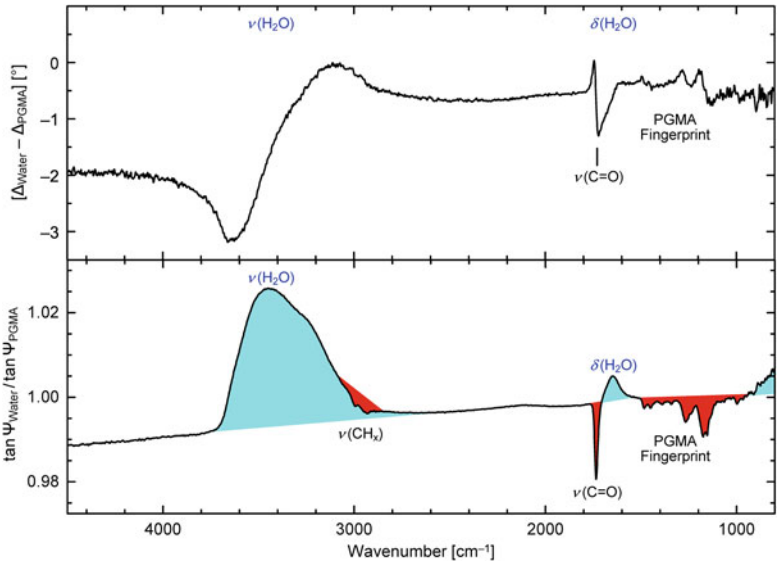

Fig. 7.16 Ellipsometric spectra of a 119 nm thick PGMA film in water referenced to spectra of a clean silicon wedge

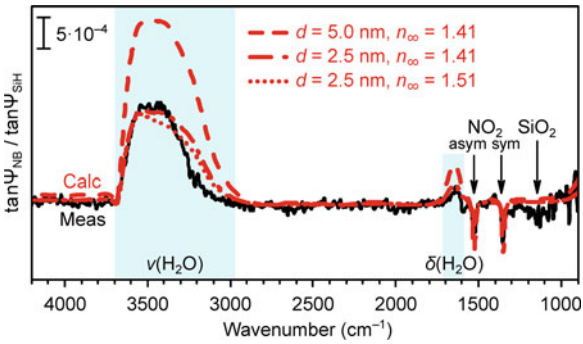

Fig. 7.17 Measured in situ tan Ψ of a nitrobenzene-modified Si surface referenced to the SiH-covered Si in the same aqueous environment prior to film grafting, compared to calculated spectra showing the sensitivity of $\nu(H_2O)$ toward changes in film thickness and refractive index. Data from [48]

and contributions from overlapping Si–OH vibrations or water molecules aligned at the charged surface—the calculations indicate the usefulness of the solvent-related bands for quantifying, e. g., film thickness.

Better agreement is usually achieved for neutral, non-charged polymer surfaces, allowing one to determine not only the thickness d_{wet} of a potentially swollen film but also to perform a fit on the film's hydration level, i. e., its water content f_{H_2O} via (7.2). This is possible even if both parameters are a priori unknown. As demonstrated in Fig. 7.18, changes in d_{wet} and f_{H_2O} lead to characteristic changes in baseline as well as water band amplitudes and shapes. $\nu(H_2O)$, for instance, scales almost linearly with d_{wet} but rather non-linearly with f_{H_2O}. Moreover, $\nu(H_2O)$ blueshifts with increasing hydration because the band is comprised of five oscillators with very strong transition

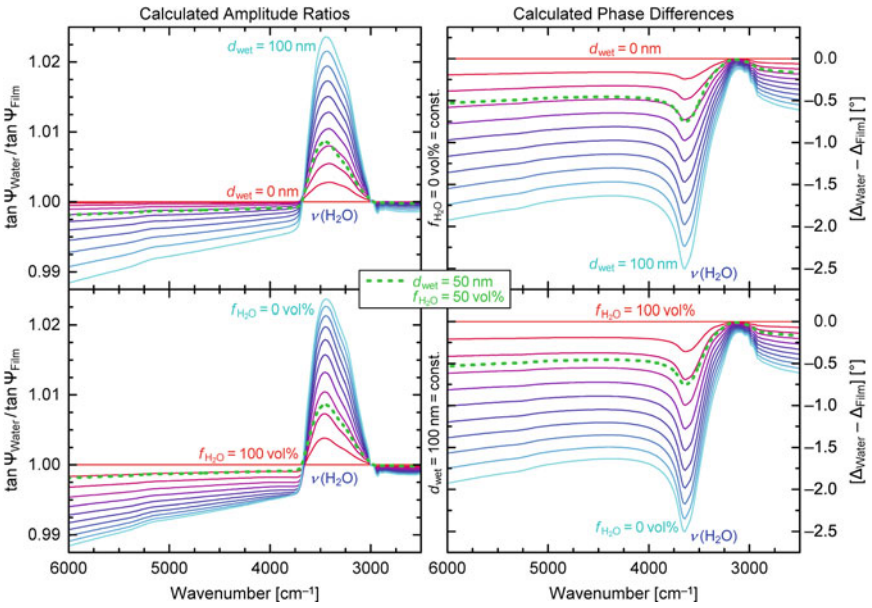

Fig. 7.18 Effects of varying film thickness d_{wet} and water content f_{H_2O} on calculated ellipsometric spectra in the $\nu(H_2O)$ region of a PGMA film on Si. Upper panels: $d_{wet} = [0, 10, \ldots, 100]$ nm with fixed $f_{H_2O} = 0$ vol%. Lower panels: $f_{H_2O} = [0, 10, \ldots, 100]$ vol% with fixed $d_{wet} = 100$ nm. Dotted lines were calculated with $d_{wet} = 50$ nm and $f_{H_2O} = 50$ vol%

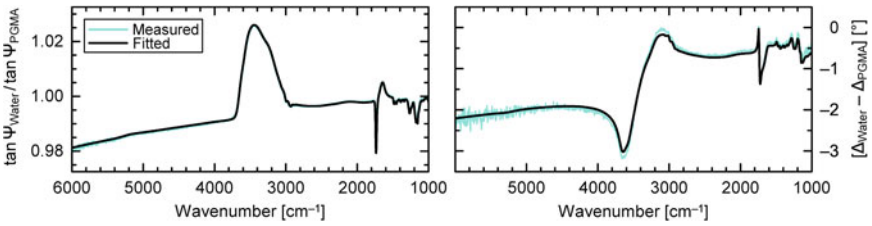

Fig. 7.19 Measured and fitted in situ IR-SE spectra of a thin PGMA film on Si in water

dipole moments [56]. Also the band shape is undergoing marked alterations upon changes in film thickness. Both effects help decorrelate d_{wet} and f_{H_2O}.

Simultaneous fits on thickness and hydration are demonstrated in Fig. 7.19 for the previously introduced 119 nm thick PGMA film. In water the film slightly swells to $d_{wet} = (123 \pm 2)$ nm with a consistently small water content of $f_{H_2O} = (5 \pm 2)\%$. Because of the film's hydrophobic nature, it is not expected that water molecules penetrate through the entirety of the film. This can be reproduced in an expanded model consisting of a non-hydrated, 70–90 nm thick sublayer and a hydrated, 30–50 nm thick toplayer, which is in agreement with AFM surface-inhomogeneity measurements that show film-thickness variations of about ±15 nm.

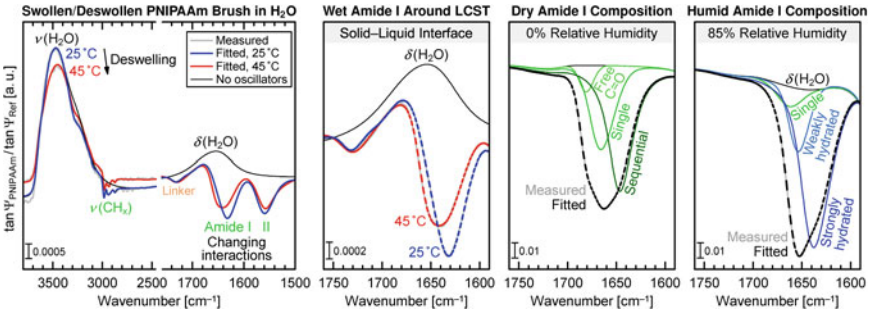

Fig. 7.20 Measured and fitted in situ IR-SE spectra of swollen and collapsed PNIPAAm films in aqueous and humid environment. Thin solid black lines are calculated spectra without polymer dielectric oscillators. For dry and humid states, individual amide I Voigt oscillator contributions are shown. Adapted with permission from [21]. Copyright (2017) American Chemical Society

7.4.4 Structure and Interactions from Quantitative In Situ IR-SE

Of course thickness and hydration are also readily accessible with VIS ellipsometry (see Chaps. 6 and 8), but one of the additional strengths of IR ellipsometry is its ability to study structural changes and molecular interactions. These effects can have considerable and distinct impacts on a vibrational spectrum, most prominently on C=O- and amide-related bands. Nikonenko et al. [57], for example, employed *ex situ* IR-SE to study mucin layers adsorbed on amphiphilic PAA-*b*-PMMA diblock copolymer surfaces. An in-depth analysis of the ν(C=O) region, the protein's amide bands, and bands related to the polymer side-chain could identify adhesive interactions and conformational changes in mucin/polymer double layers. Different components of the C=O stretching bands revealed hydrogen bonds between mucin and polymer without the participation of the mucin's amide groups. From an amide I component analysis, an increase in the proportion of beta-sheets was observed, indicating a more unfolded and aggregated structure of mucin after adsorption.

The obvious aim is to perform such revealing band analyses in situ with the polymer films in contact with aqueous environments. For this purpose, optical modeling of in situ IR-SE spectra is employed based on the Bruggeman effective-medium approximation and a set of vibrational oscillators that describes the differently interacting and non-interacting molecular groups. The detailed example presented is again that of polymer brushes made from PNIPAAm, a temperature-responsive model polymer with regard to structure and interactions of peptides and proteins.

PNIPAAm films measured in aqueous, dry, and humid ambient conditions give rise to rich vibrational spectra [21], as can be seen in Fig. 7.20. Virtually all bands are affected by the presence of water within the film, most noticeably the $\nu(H_2O)$ region and the polymer-related amide and alkyl-stretching bands. While changes in the $\nu(H_2O)$ bands are directly related to swelling and hydration effects, band alterations

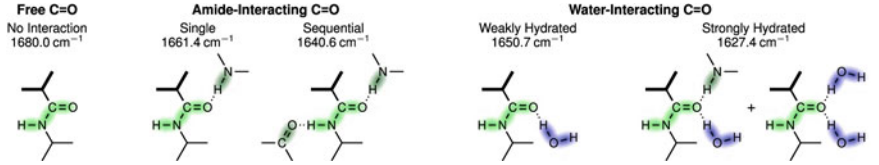

Fig. 7.21 Carbonyl–amide and carbonyl–water hydrogen-bond interactions in PNIPAAm polymer brushes. Stated wavenumbers refer to fitted amide I oscillator frequencies in the optical model. Adapted with permission from [21]. Copyright (2017) American Chemical Society

in the amide region are evidence for changing molecular interactions associated with PNIPAAm's amide side groups.

Focusing on the tan Ψ amide I band, a second-derivative analysis indicates several subbands, which are related to the various hydrogen-bond interactions depicted in Fig. 7.21. PNIPAAm's C=O moieties can be free (i. e., non-interacting), or involved in intramolecular carbonyl–amide or intermolecular carbonyl–water interactions. Corresponding carbonyl stretching oscillators are progressively redshifted with increasing number and strength of hydrogen bonds [58], and are sufficiently well-separated to allow their accurate determination with IR-SE.

Fitting the data allows a comprehensive analysis of film hydration, interactions, and swelling [21]. Figure 7.22 plots the relative fractions of differently interacting C=O species, the hydration-sensitive oscillator position of antisymmetric methyl stretching, as well as film swelling and number of water molecules per PNIPAAm monomer—all in dependence of the film's water content, as fitted using the Bruggeman equation (7.2). In dry state, the film is dominated by sequentially hydrogen-bonded amide groups, similar to alpha-helices in proteins. Expectedly, amide–amide interactions are replaced by amide–water interactions as the film hydrates in humid air. Approaching 85% relative humidity, all free carbonyl groups become hydrated, while weakly hydrated C=O groups are more and more converted to strongly hydrated ones. At 25 °C in water, the brush is highly swollen and hydrated. In fact, the majority of carbonyl groups is strongly hydrated, with only a few groups remaining involved in pure hydrogen bonds with neighboring amide groups. At 45 °C in water, the brush deswells and dehydrates, with a small percentage of carbonyl groups becoming dehydrated and/or incorporated into sequential amide–amide bonds again. This conversion from amide–water- to amide–amide-interacting carbonyl groups, although expected, leaves most C=O groups unaffected and strongly hydrated, which is in accordance with the considerable amount of water (52 vol%) retained within the collapsed brush. Comparing C=O fractions and swelling behavior, it can be concluded that additional water molecules above 25 vol% water content do not necessarily contribute to specific interactions with PNIPAAm's amide groups, but rather to the overall brush hydration. This hydration is also observed in the $\nu_{as}(CH_3)$ band position corresponding to the polymer's hydrophobic isopropyl side groups.

Interestingly, there was no detectable preferential molecular orientation, neither in the collapsed nor in the stretched state. An isotropic distribution of orientations seems

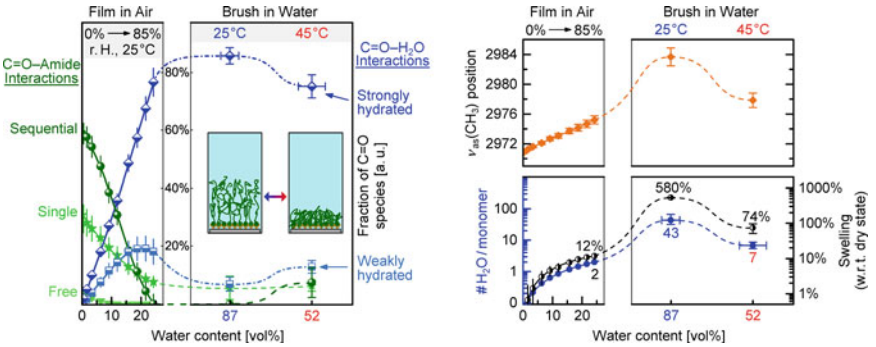

Fig. 7.22 Humidity- and temperature-dependent interactions, hydration states, and structure of PNIPAAm films. Left: Amide–amide and amide-water interactions of hydrophilic carbonyl groups. Right-top: Hydration of hydrophobic isopropyl groups. Right-bottom: Number of water molecules per monomer and film swelling with respect to dry-state thickness. Adapted with permission from [21]. Copyright (2017) American Chemical Society

reasonable because the chains are still far away from being completely stretched, even in the brush's highly swollen state.

It has been shown in this section that IR-SE on solid–liquid interfaces can deliver detailed qualitative and quantitative information about the physical and chemical properties of polymer thin films in aqueous environments. Being able to monitor the films while applying external stimuli revealed fascinating surface characteristics. Such investigations are highly interesting for complex polymer film systems like adsorbed peptides, proteins, or membranes.

7.5 Future Prospects

This chapter gave an overview of the many uses of infrared ellipsometry for studies of thin polymer films, in particular with regard to investigations of structure and molecular interactions. Current trends in IR-SE are focusing on improving three major aspects of the method: spatial resolution, temporal resolution, and information content. The latter is being addressed, for instance, by infrared Mueller ellipsometry [59, 60]. This generalized version of IR-SE can probe a sample's complete 4×4 Mueller matrix, thus allowing deeper insights into the properties of depolarizing and anisotropic nanostructured polymer films.

Lateral and temporal resolution are addressed with ellipsometric techniques that make use of brilliant light sources much brighter than standard IR globars (see Chap. 22). Synchrotron IR-SE, for example, was used for mapping chemical composition and dissociation of 3 nm ultrathin pH-responsive PAA brushes with a spatial resolution of $300\times800\ \mu m^2$ [61]. A similar mapping study employed in situ

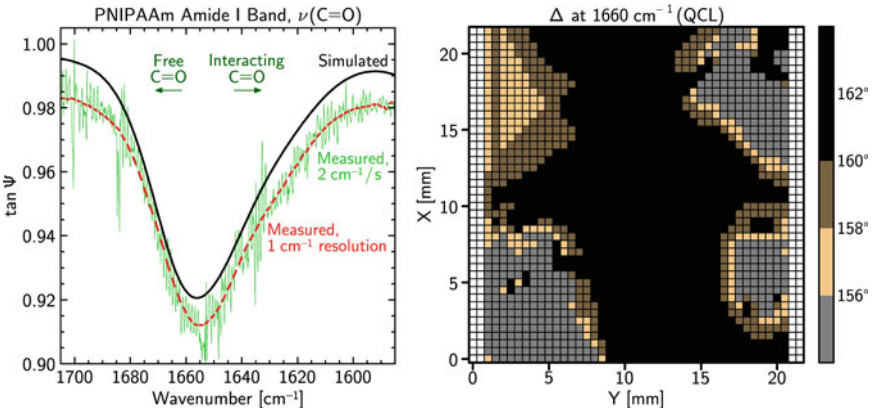

Fig. 7.23 Inhomogeneous, 90 nm thick PNIPAAm film on gold measured with IR laser ellipsometry. Left: QCL tan Ψ sweeps compared to a simulated spectrum (top) determined from conventional ellipsometry. Right: Δ homogeneity map of the film's amide I band. Adapted from [65]. Copyright (2017), with permission from Elsevier

synchrotron IR-SE on binary PAA-*b*-PS/PEG brushes in aqueous environments between pH 2 and 10 for determining carboxyl dissociation and film homogeneity [62].

Another interesting approach is IR-ellipsometric microscopy [63, 64] based on commercial reflection/transmission microscopes. Here, the set-up's Cassegrain objective is expanded by two polarizers and a plane-of-incidence defining aperture enabling IR-SE measurements with resolutions down to the diffraction limit. For films of a few 10 nm thickness, measurements with spot sizes of 40×40 μm^2 have been demonstrated, enabling straightforward IR-SE mapping of vibrational bands.

IR laser ellipsometry has recently been introduced and—utilizing tunable quantum cascade lasers (QCLs)—advanced toward spectral studies and mapping characterization of thin polymer films with per-spot resolutions of 60 ms and 120×250 μm^2 [65, 66]. An example is given in Fig. 7.23 showing the amide I region of a 90 nm thick, inhomogeneous PNIPAAm film spectrally measured within seconds and mapped within minutes.

The limits of both lateral and temporal resolution are further pushed by yet another novel technique termed IR nanopolarimetry [67]. Utilizing broad-bandwidths QCLs and a polarization control, this AFM-based method probes a film's frequency-dependent thermal expansion, hence providing direct measurements of IR absorption in domains as small as a few (10 nm)^2. IR nanopolarimetry was successfully used to characterize anisotropic porphyrin supramolecular assemblies, revealing that the aggregate's morphology can be correlated with anisotropic organization and hence different oriented attachment growth mechanisms.

All of the aforementioned techniques hold a bright future for IR-SE characterization of polymer thin films. Temporally improved, nanoscale-resolved measurements will increasingly facilitate kinetic studies of nanostructure and interactions, which

is of great importance for film preparation, characterization, process control, and applications.

References

1. V.P. Tolstoy, I.V. Chernyshova, V.A. Skryshevsky, *Handbook of Infrared Spectroscopy of Ultrathin Films* (Wiley, Chichester, 2003)
2. J.M. Chalmers, P.R. Griffiths, *Handbook of Vibrational Spectroscopy* (Wiley, Chichester, 2006)
3. N. Everall, P.R. Griffiths, J.M. Chalmers, *Vibrational Spectroscopy of Polymers: Principles and Practice* (Wiley, Chichester, 2007)
4. S. Thomas, Y. Grohens, P. Jyotishkumar, *Characterization of Polymer Blends: Miscibility, Morphology and Interfaces* (Wiley-VCH Verlag GmbH & Co, KGaA, 2015)
5. R.T. Graf, F. Eng, J.L. Koenig, H. Ishida, Appl. Spectrosc. **40**, 498–503 (1986)
6. C.L. Bungay, T.E. Tiwald, D.W. Thompson, M.J. DeVries, J.A. Woollam, J.F. Elman, Thin Solid Films **313–314**, 713–717 (1998)
7. T. Heitz, B. Drévillon, J.E. Bourée, C. Godet, J. Non-Cryst, Solids **227–230**, 636–640 (1998)
8. D. Blaudez, F. Boucher, T. Buffeteau, B. Desbat, M. Grandbois, C. Salesse, Appl. Spectrosc. **53**, 1299–1304 (1999)
9. K. Hinrichs, D. Tsankov, E.H. Korte, A. Röseler, K. Sahre, K.-J. Eichhorn, Appl. Spectrosc. **56**, 737–743 (2002)
10. M. Schubert, C. Bundesmann, G. Jakopic, H. Maresch, H. Arwin, N.-C. Persson, F. Zhang, O. Inganäs, Thin Solid Films **455–456**, 295–300 (2004)
11. H.G. Tompkins, T. Tiwald, C. Bungay, A.E. Hooper, J. Phys. Chem. **108**, 3777–3780 (2004)
12. A. Laskarakis, S. Logothetidis, J. Appl. Phys. **99**, 066101 (2006)
13. W.R. Folks, S.K. Pandey, G. Pribil, D. Slafer, M. Manning, G. Boreman, Int. J. Infrared Milli. Waves **27**, 1553–1571 (2006)
14. J.L. Stehle, J.P. Piel, Appl. Surf. Sci. **256S**, S72–S76 (2009)
15. S. Kang, V.M. Prabhu, C.L. Soles, E.K. Lin, W. Wu, Macromolecules **42**, 5296 (2009)
16. H. Arwin, Thin Solid Films **519**, 2589–2592 (2011)
17. D. De Sousa Meneses, G. Gruener, M. Malki, P. Echegut, J. Non-Cryst. Solids **351**, 124–129 (2005)
18. F. Schreier, D. Kohlert, Comput. Phys. Commun. **179**, 457–465 (2008)
19. D.A.G. Bruggeman, Ann. Phys. (Berlin, Ger.) **416**, 636–664 (1935)
20. D.E. Aspnes, Thin Solid Films **89**, 249–262 (1982)
21. A. Furchner, A. Kroning, S. Rauch, P. Uhlmann, K.-J. Eichhorn, K. Hinrichs, Anal. Chem. **89**, 3240–3244 (2017)
22. J. Klein, Science **250**, 640–646 (1990)
23. S. Mavila, O. Eivgi, I. Berkovich, N.G. Lemcoff, Chem. Rev. **116**, 878–961 (2016)
24. K. Hinrichs, M. Gensch, N. Nikonenko, J. Pionteck, K.-J. Eichhorn, Macromol. Symp. **230**, 26–32 (2005)
25. N. Nikonenko, K. Hinrichs, E.H. Korte, J. Pionteck, K.-J. Eichhorn, Macromolecules **37**, 8661–8667 (2004)
26. P. Duckworth, H. Richardson, C. Carelli, J.L. Keddie, Surf. Interface Anal. **36**, 33–41 (2004)
27. L. Ionov, A. Sidorenko, K.-J. Eichhorn, M. Stamm, S. Minko, K. Hinrichs, Langmuir **21**, 8711–8716 (2005)
28. K.L., Y. Gu, H. Zhang, Z. Qiang, B.D. Vogt, N.S. Zacharia, Langmuir **32**, 9118–9125 (2016)
29. T.R.E. Simpson, J.L. Keddie, J. Adhes. **79**, 1207–1218 (2003)
30. A. Ulman, Chem. Rev. **96**, 1533–1554 (1996)
31. J.C. Love, L.A. Estroff, J.K. Kriebel, R.G. Nuzzo, G.M. Whitesides, Chem. Rev. **105**, 1103–1169 (2005)

32. M.D. Porter, T.B. Bright, D.L. Allara, C.E.D. Chidsey, J. Am. Chem. Soc. **109**, 3559–3568 (1987)
33. M.M. Walczak, C. Chung, S.M. Stole, C.A. Widrig, M.D. Porter, J. Am. Chem. Soc. **113**, 2370–2378 (1991)
34. Z.G. Hu, P. Prunici, P. Patzner, P. Hess, J. Phys. Chem. B **110**, 14824–14831 (2006)
35. D.M. Rosu, J.C. Jones, J.W.P. Hsu, K.L. Kavanagh, D. Tsankov, U. Schade, N. Esser, K. Hinrichs, Langmuir **25**, 919–923 (2009)
36. D.L. Allara, R.G. Nuzzo, Langmuir **1**, 52–66 (1985)
37. R. Arnold, A. Terfort, C. Wöll, Langmuir **17**, 4980–4989 (2001)
38. D. Tsankov, K. Hinrichs, E.H. Korte, R. Dietel, A. Röseler, Langmuir **18**, 6559–6564 (2002)
39. E.H. Korte, K. Hinrichs, A. Röseler, Spectrochim. Acta B **57**, 1625–1634 (2002)
40. K. Hinrichs, M. Levichkova, D. Wynands, K. Walzer, K.-J. Eichhorn, P. Bäuerle, K. Leo, M. Riede, Thin Solid Films **525**, 97–105 (2012)
41. A. Kroning, A. Furchner, D. Aulich, E. Bittrich, S. Rauch, P. Uhlmann, K.-J. Eichhorn, M. Seeber, I. Luzinov, S.M. Kilbey II, B.S. Lokitz, S. Minko, K. Hinrichs, A.C.S. Appl, Mater. Interfaces **7**, 12430–12439 (2015)
42. D. Aulich, O. Hoy, I. Luzinov, M. Brücher, R. Hergenröder, E. Bittrich, K.-J. Eichhorn, P. Uhlmann, M. Stamm, N. Esser, K. Hinrichs, Langmuir **26**, 12926–12932 (2010)
43. A. Kroning, A. Furchner, S. Adam, P. Uhlmann, K. Hinrichs, Biointerphases **11**, 019005 (2016)
44. Y. Mikhaylova, L. Ionov, J. Rappich, M. Gensch, N. Esser, S. Minko, K.-J. Eichhorn, M. Stamm, K. Hinrichs, Anal. Chem. **79**, 7676–7682 (2007)
45. K. Hinrichs, D. Aulich, L. Ionov, N. Esser, K.-J. Eichhorn, M. Motornov, M. Stamm, S. Minko, Langmuir **25**, 10987–10991 (2009)
46. G. Sun, X. Zhang, C. Kaspari, K. Haberland, J. Rappich, K. Hinrichs, J. Electrochem. Soc. **159**, H811–H815 (2012)
47. O. Hoy, B. Zdyrko, R. Lupitskyy, R. Sheparovych, D. Aulich, J. Wang, E. Bittrich, K.-J. Eichhorn, P. Uhlmann, K. Hinrichs, M. Müller, M. Stamm, S. Minko, I. Luzinov, Adv. Funct. Mater. **20**, 2240–2247 (2010)
48. J. Rappich, K. Hinrichs, Electrochem. Commun. **11**, 2316–2319 (2009)
49. P. Kanyong, G. Sun, F. Rösicke, V. Syritski, U. Panne, K. Hinrichs, J. Rappich, Electrochem. Commun. **512**, 103–107 (2015)
50. G. Sun, X. Zhang, J. Rappich, K. Hinrichs, Appl. Surf. Sci. **344**, 181–187 (2015)
51. A. Furchner, E. Bittrich, P. Uhlmann, K.-J. Eichhorn, K. Hinrichs, Thin Solid Films **541**, 41–45 (2013)
52. E. Bittrich, S. Burkert, M. Müller, K.-J. Eichhorn, M. Stamm, P. Uhlmann, Langmuir **28**, 3439–3448 (2012)
53. S. Adam, M. Koenig, K.B. Rodenhausen, K.-J. Eichhorn, U. Oertel, M. Schubert, M. Stamm, P. Uhlmann, Appl. Surf. Sci. **421**, 843–851 (2017)
54. P.R. Griffiths, James A. De, J.D.Winefordner Haseth, *Fourier Transform Infrared Spectrometry* (Wiley, Chichester, 2007)
55. M. Miljkovič, B. Bird, M. Diem, Analyst **137**, 3954–3964 (2012)
56. J.-J. Max, C. Chapados, J. Phys. Chem. A **106**, 6452–6461 (2002)
57. N.A. Nikonenko, I.A. Bushnak, J.L. Keddie, Appl. Spectrosc. **63**, 889–898 (2009)
58. A. Barth, Biochim. Biophys. Acta, Bioenerg. **1767**, 1073–1101 (2007)
59. E. Garcia-Caurel, A. Lizana, G. Ndong, B. Al-Bugami, C. Bernon, E. Al-Qahtani, F. Rengnez, A. de Martino. Appl. Opt. **56**, 2776–2785 (2015)
60. G. Ndong, A. Lizana, E. Garcia-Caurel, V. Paret, G. Melizzi, D. Cattelan, B. Pelissier, J.H. Tortai, Appl. Opt. **55**, 3323–3332 (2016)
61. K. Roodenko, Y. Mikhaylova, L. Ionov, M. Gensch, M. Stamm, S. Minko, U. Schade, K.-J. Eichhorn, N. Esser, K. Hinrichs, Appl. Phys. Lett. **92**, 103102 (2008)
62. D. Aulich, O. Hoy, I. Luzinov, K.-J. Eichhorn, M. Stamm, M. Gensch, U. Schade, N. Esser, K. Hinrichs, Phys. Status Solidi C **7**, 197–199 (2010)
63. K. Hinrichs, A. Furchner, J. Rappich, T.W.H. Oates, J. Phys. Chem. C **117**, 13557–13563 (2013)

64. K. Hinrichs, A. Furchner, G. Sun, J. Rappich, M. Gensch, T.W.H. Oates, Thin Solid Films **571**, 648–652 (2014)
65. A. Furchner, C. Kratz, D. Gkogkou, H. Ketelsen, K. Hinrichs, Appl. Surf. Sci. **421**, 440–445 (2017)
66. A. Furchner, G. Sun, H. Ketelsen, J. Rappich, K. Hinrichs, Analyst **140**, 1791–1797 (2015)
67. T. Shaykhutdinov, S.D. Pop, A. Furchner, K. Hinrichs, ACS Macro Lett. **6**, 598–602 (2017)